Radiology

3D Super-Resolution US Imaging of Rabbit Lymph Node Vasculature in Vivo by Using Microbubbles

Jiaqi Zhu, MEng • Ethan M. Rowland, PhD • Sevan Harput, PhD • Kai Riemer, MSc • Chee Hau Leow, PhD • Brett Clark, BSc • Karina Cox, MD • Adrian Lim, MD • Kirsten Christensen-Jeffries, PhD • Ge Zhang, MSc • Jemma Brown, MSc • Christopher Dunsby, PhD • Robert J. Eckersley, PhD • Peter D Weinberg, PhD • Meng-Xing Tang, PhD

From the Department of Bioengineering, Imperial College London, South Kensington Campus, London SW7 2AZ, England (J.Z., E.M.R., S.H., K.R., C.H.L., G.Z., P.D.W., M.X.T.); Department of Surgery, Maidstone and Tunbridge Wells NHS Trust, Maidstone, England (K.C.); Department of Imaging, Charing Cross Hospital, Fulham Palace Rd, London, England (A.L.); Department of Biomedical Engineering, School of Biomedical Engineering and Imaging Science, Kings College London, London, England (K.C.J., J.B., R.J.E.); Department of Physics and Centre for Pathology, Imperial College London, London, England (C.D.); and Department of Imaging, Natural History Museum, London, England (B.C.). Received November 11, 2018; revision requested January 9, 2019; final revision received February 5; accepted February 28. **Address correspondence to** M.X.T. (e-mail: *mengxing.tang@imperial.ac.uk*).

Supported in part by Engineering and Physical Sciences Research Council under grant nos. EP/N015487/1, EP/N014855/1, and EP/M011933/1; Cancer Research UK Multidisciplinary Project Award under grant no. C53470/A22353; Imperial Confidence-in-Concepts; Imperial Proof-of-Concept; and British Heart Foundation Centre of Research Excellence.

K.R. and P.D.W. supported by British Heart Foundation.

Conflicts of interest are listed at the end of this article.

Radiology 2019; 291:642–650 • https://doi.org/10.1148/radiol.2019182593 • Content code: US

Background: Variations in lymph node (LN) microcirculation can be indicative of metastasis. The identification and quantification of metastatic LNs remains essential for prognosis and treatment planning, but a reliable noninvasive imaging technique is lacking. Three-dimensional super-resolution (SR) US has shown potential to noninvasively visualize microvascular networks in vivo.

Purpose: To study the feasibility of three-dimensional SR US imaging of rabbit LN microvascular structure and blood flow by using microbubbles.

Materials and Methods: In vivo studies were carried out to image popliteal LNs of two healthy male New Zealand white rabbits aged 6–8 weeks. Three-dimensional, high-frame-rate, contrast material–enhanced US was achieved by mechanically scanning with a linear imaging probe. Individual microbubbles were identified, localized, and tracked to form three-dimensional SR images and super-resolved velocity maps. Acoustic subaperture processing was used to improve image contrast and to generate enhanced power Doppler and color Doppler images. Vessel size and blood flow velocity distributions were evaluated and assessed by using Student paired *t* test.

Results: SR images revealed microvessels in the rabbit LN, with branches clearly resolved when separated by 30 μm, which is less than half of the acoustic wavelength and not resolvable by using power or color Doppler. The apparent size distribution of most vessels in the SR images was below 80 μm and agrees with micro-CT data, whereas most of those detected with Doppler techniques were larger than 80 μm in the images. The blood flow velocity distribution indicated that most of the blood flow in rabbit popliteal LN was at velocities lower than 5 mm/sec.

Conclusion: Three-dimensional super-resolution US imaging using microbubbles allows noninvasive nonionizing visualization and quantification of lymph node microvascular structures and blood flow dynamics with resolution below the wave diffraction limit. This technology has potential for studying the physiologic functions of the lymph system and for clinical detection of lymph node metastasis.

Online supplemental material is available for this article.

The lymphatic system plays an important role in human circulatory and immune homeostasis. Peripheral lymph nodes (LNs) are regional hubs that receive interstitial fluid as well as circulating blood. They contain large numbers of immune cells and the complex internal architecture of LNs constitutes an interface between the cellular and molecular constituents of lymph and blood. Cellular debris is filtered and primary immune responses can be generated in LNs to pathogens (1). LN blood vessels are highly specialized for facilitating T-cell entry to the node (2). The spatial distribution of surface area for exchange of fluid with blood vessels in LNs determines the amount of local fluid movement, and it is therefore important to quantify the three-dimensional distribution of LN blood vessels.

In patients with cancer, tumor cells can also traffic through lymphatic channels to regional LNs (3). Recent studies have demonstrated that metastatic cells migrate toward and into LN blood vessels (4,5). Malignant processes are associated with both angiogenesis and lymphangiogenesis (6). LNs may even act as a permissive niche to support the proliferation of metastatic cells and promote movement to distant sites (7). The accurate identification and quantification of metastatic LNs remains essential for prognosis and treatment planning (8).

Abbreviations

ASAP = acoustic subaperture processing, LN = lymph node, PD = power Doppler, SR = super-resolution

Summary

By using microbubbles, three-dimensional super-resolution US in vivo imaging of rabbit lymph nodes visualizes the complex microvascular network and blood flow dynamics with a resolution well beyond the wave diffraction limit, giving the ability to resolve microvessels 30 μm apart.

Key Points

- Three-dimensional super-resolution (SR) US imaging with microbubble contrast agents noninvasively visualized rabbit lymph node (LN) microvessels and quantified blood flow dynamics in vivo with a 15-fold improvement in resolution compared with color or power Doppler.
- Three-dimensional SR US imaging was able to resolve individual microvessels in LNs separated by 0.03 mm.
- The velocity distribution indicated that most of the blood flow in LNs was at velocities lower than 5 mm/sec.

US (9), x-ray imaging, CT, PET, and MRI have replaced invasive lymphangiography (10) and have been widely used clinically for noninvasive assessment of LNs. However, the usefulness of the images is restricted by their relatively low spatial resolution and contrast.

Super-resolution (SR) US imaging is the acoustic counterpart of optical SR. SR US overcomes the compromise in conventional US imaging between spatial resolution and penetration depth. In SR US imaging, microbubbles are considered point scatterers as their size (typically 1–7 μm) is much smaller than is the US wavelength. Spatially isolated microbubbles are localized and accumulated through multiple acquired frames to reconstruct the final SR image. Several research groups have demonstrated this technique by using different in vitro (11,12) and in vivo (13–17) models, in humans (18–20), and by using nanodroplets (21).

Three-dimensional US has the potential to improve both qualitative inspection and the accuracy of quantitative approaches when imaging the complex architecture of vascular networks. It can be obtained with mechanical scanning to acquire a stack of two-dimensional SR images (14,22). SR in all three directions was achieved through the use of two one-dimensional transducer arrays (12,23) or a hemispherical array probe (24).

In this study, we hypothesized that microvessel network and flow dynamics can be noninvasively visualized in rabbit LNs with a resolution beyond the wave diffraction limit in vivo by using SR US imaging and microbubbles as contrast agents.

Materials and Methods

Animals

New Zealand rabbits (n = 2) were used in this study in March and August 2018. All animal experiments complied with the Animals (Scientific Procedures) Act 1986 and were approved by the local ethical review panel. Two specific pathogen-free male rabbits (HSDIF strain; Envigo, Hillcrest, United Kingdom) aged 6–8 weeks were individually housed in pens at 18–22°C (64.4–71.6°F) on a 12-hour light period and were fed a standard laboratory diet (25).

In Vivo Protocol

Fentanyl and fluanisone (0.3 mL/kg) and midazolam (0.025 mL/kg) were administered through the marginal vein of each rabbit to produce general anesthesia. Maintenance doses were given as required. The rabbits were placed on a warming pad to maintain body temperature at 37°C (98.6°F) and artificially ventilated. Fur on the legs of the rabbits was removed and Evans blue dye (0.1 mL of a 1% wt/vol solution) was injected subcutaneously into the rear footpad to label the lymphatic drainage of the hind leg. Gentle massage was administrated on the leg and rear footpad to accelerate the flow of the dye into the popliteal LN. Five to 10 minutes later, 0.5 mL of lignocaine was injected subcutaneously, skin at the back of the knee was reflected, and the blue-labeled lymphatic channels and popliteal LN were identified.

US Imaging

To perform three-dimensional, high-frame-rate, contrast material–enhanced US acquisition, a Verasonics system (Vantage 256; Verasonics, Kirkland, Wash) was synchronized with a mechanical scanning system (12-mm motorized translation stage; Thorlabs, Exter, United Kingdom) to translate a one-dimensional array transducer (L22-14v; Verasonics) along the elevation direction. Figure E1 (online) shows the experiment and experimental system. The total scanning distance was 1.7 mm with a step size of 100 μm, reflecting a balance between acquisition time and quality of volume reconstruction.

Plane waves with 15 inclination angles between −7.5° and 7.5° were transmitted at a pulse repetition frequency of 25 kHz to obtain coherently compounded B-mode images at a frame rate of 500 Hz. For each angle, a single-cycle plane-wave pulse was transmitted at 18 MHz and a mechanical index of 0.1. For each scanning position, 1200 compounded B-mode images were acquired. Each scan took 2.4 sec and the total scanning time was 40.8 sec.

Contrast Agents

Contrast agents used in this study were in-house–manufactured gas-filled microbubbles with an average size of 1 μm and a concentration of 5×10^9 microbubbles per milliliter. Their fabrication and size distribution are described in Lin et al (26). Every 2 minutes, a 0.1-mL bolus was introduced through the marginal ear vein. This time interval was chosen to maintain a microbubble concentration that gave an acceptable signal-to-noise ratio together with sufficient isolated microbubbles for SR processing.

Doppler Processing

Power Doppler (PD) and color Doppler images were generated off-line from the same data. Acoustic subaperture processing (ASAP) (27) was used to enhance contrast in PD and color Doppler images. In ASAP, the received US channel data are split into two subgroups and the reconstructed data from the subgroups are temporally correlated over frames to generate fi-

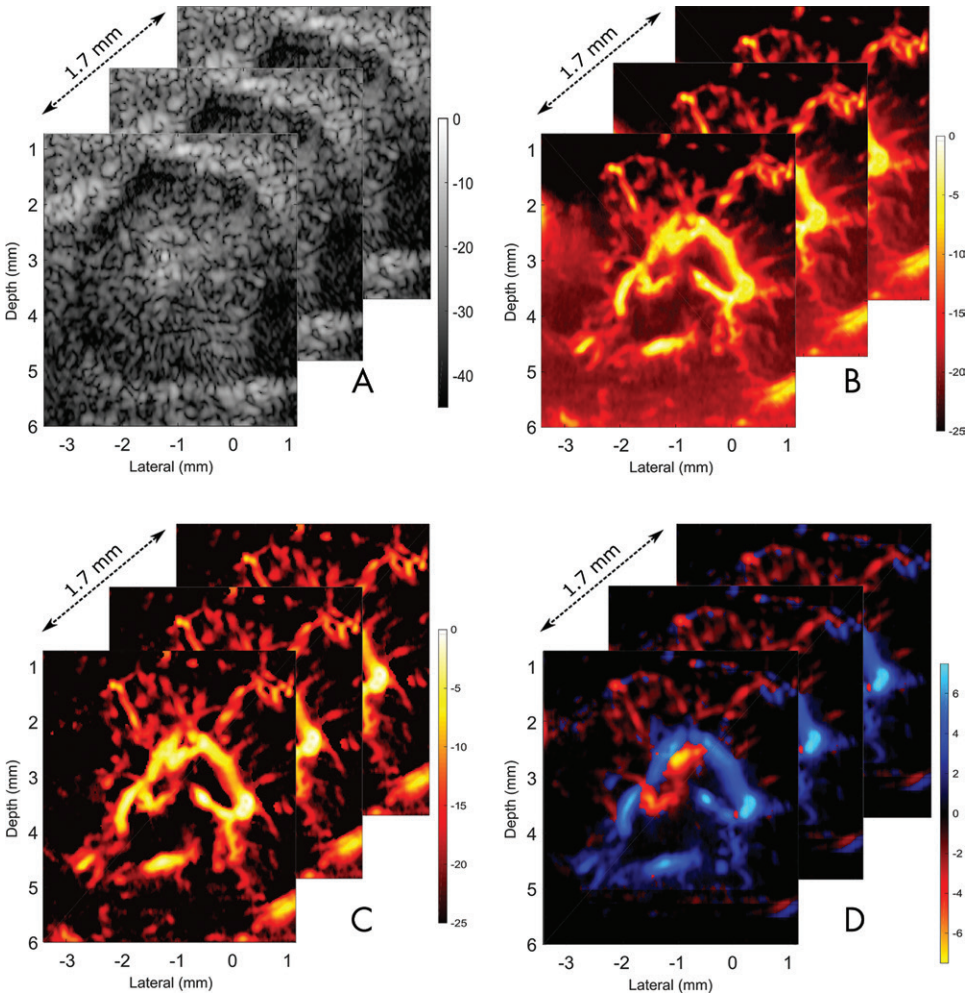

Figure 1: Images show two-dimensional section of popliteal lymph node. *A, E,* B-mode images, *B, F,* power Doppler (PD) images, *C, G,* acoustic subaperture processing (ASAP)–enhanced PD images,
(Fig 1 continues)

nal images with reduced noise. Three-dimensional projection of SR images and ASAP-enhanced PD images were generated by combining information from 17 scanning positions, projecting the maximum intensity for each pixel over the 17 positions.

SR US Imaging

SR images were obtained through off-line postprocessing of the acquired image sequences. We initially estimated an intensity threshold that represented the noise level from all acquired frames. We then detected microbubble regions with pixel intensity higher than the threshold. Features of detected regions such as shape, intensity, and size were compared with the point spread function acquired from a characterization experiment in which a 30-μm wire target was imaged with the same imaging parameters and settings used in the animal experiments. We rejected regions not consistent with the point spread function, which were mainly associated with noise or multiple bubbles signals. The intensity-weighted centers of mass of detected regions were then calculated as centroid positions. These were accumulated from all image frames to generate SR images (13). Each centroid position was represented by a Gaussian profile with standard deviation of 10 μm, given by the localization precision.

Additionally, each moving isolated microbubble (Movies E1, E2 [online]) was tracked locally (13). Blood flow velocity and direction were determined by using this tracking algorithm and presented with color scales in SR velocity maps.

Quantitative Evaluation

Spatial resolution of the SR images was evaluated off-line by quantifying the distance between separable microvessels in a region of interest. The same region of interest was selected on the equivalent ASAP-enhanced PD image for comparison.

Multiscale Hessian vessel enhancement based on Frangi vessel function was used to quantify vessel sizes in images (28–30) for both ASAP-enhanced PD images and SR images.

Micro-CT Scan

A micro-CT scan was performed to image a vascular corrosion cast of a third rabbit LN. The distribution of vessel sizes was obtained from the resulting three-dimensional topology. Detailed methods are given in Appendix E1 (online).

Statistical Analysis

Histograms of vessel size distribution were generated off-line and significance of the difference in imaged vessel sizes between SR and PD was assessed by using Student paired *t* test over 17 sections from each of the two rabbits by the ttest function in the open-source software Matlab (version R2016a; Natick, Mass). $P < .001$ was considered to indicate statistically significant difference. Histogram of flow velocity distribution was also generated off-line.

Results

ASAP-enhanced PD Images

Figure 1 shows two-dimensional grayscale US images and corresponding PD images and ASAP-enhanced Doppler images from the two rabbits. The B-mode image in Figure 1, *A* shows the diameters of the LNs to be 4 mm (top) and 3 mm (bottom). In Figure 1, *B* and *C*, the intranodal vessels are visualized and the ASAP-enhanced PD images have a substantially

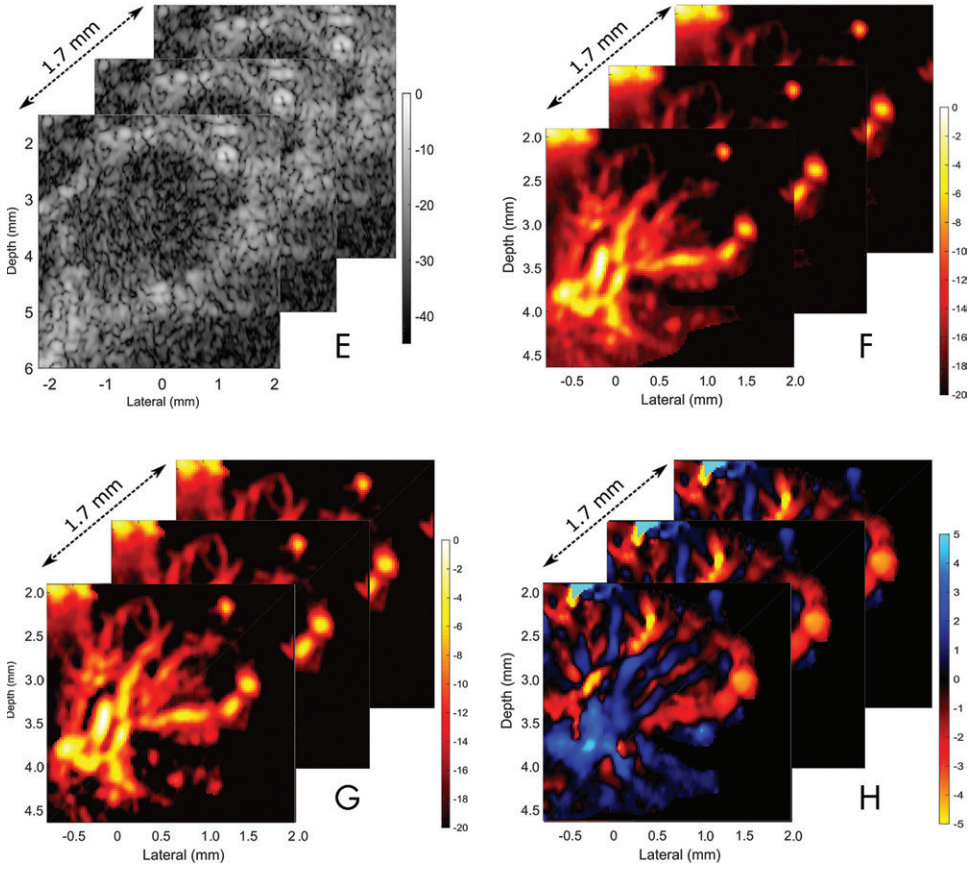

Figure 1 *(continued)*: and *D, E,* ASAP-enhanced color Doppler images. Top and bottom groups of images were obtained from two different lymph nodes.

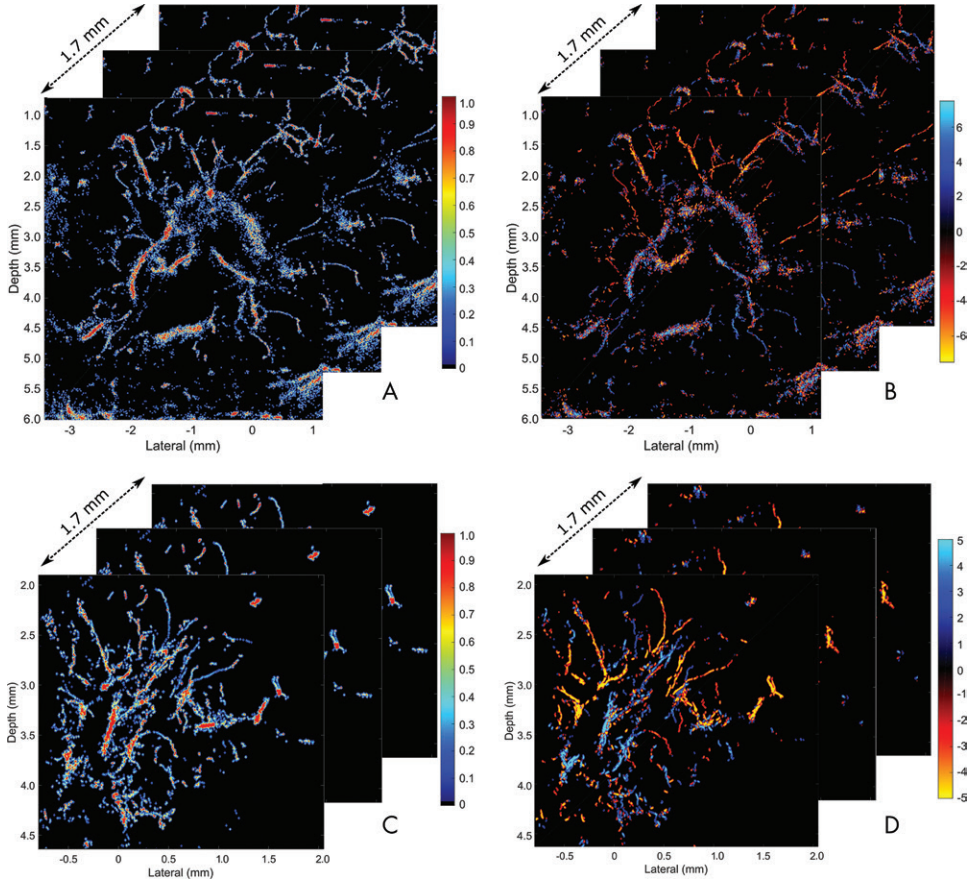

Figure 2: Images show two-dimensional section of popliteal lymph node. *A,C,* On super-resolution (SR) images, color bar corresponds to normalized number of localized microbubbles. *B, D,* On SR velocity maps, blue indicates flow going toward transducer and red indicates flow going away from transducer. Top and bottom groups of images were obtained from two different lymph nodes.

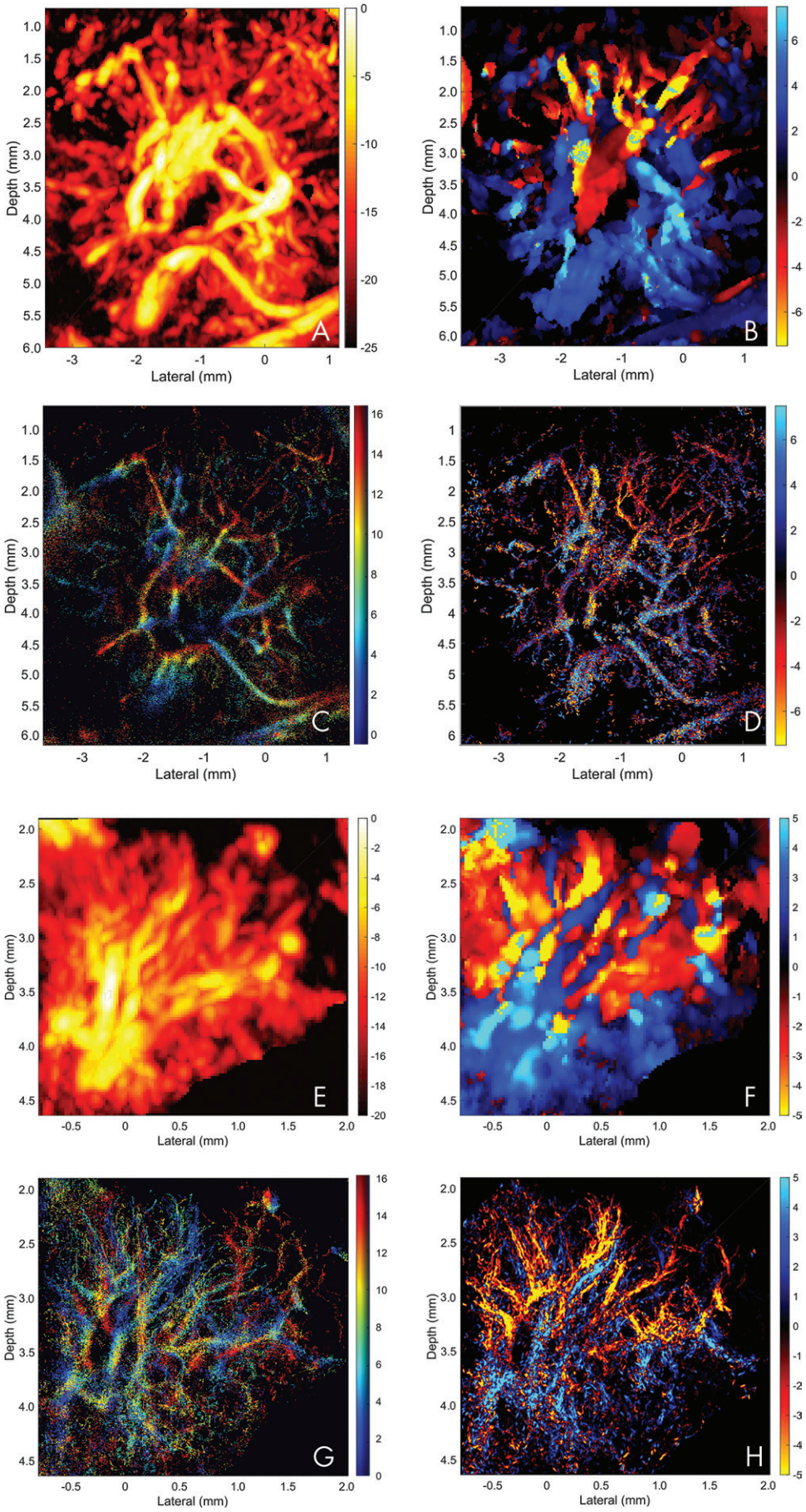

Figure 3: Images show two-dimensional projection of popliteal lymph node through 17 imaging sections covering 1.7-mm thickness. *A,* Maximum intensity projection (MIP) of acoustic subaperture processing (ASAP)–enhanced power Doppler (PD) images. *B,* MIP of ASAP-enhanced color Doppler (CD) images. *C,* On depth color-coded super-resolution (SR) MIP images, hue encodes image section with maximum intensity and saturation represents number of microbubbles localized at that depth. *D,* On velocity color-coded MIP, color shows velocity and direction. *A–D* are obtained from same rabbit lymph node by using same acquired data but different postprocessing, and *E–H* show same types of images but from different lymph node.

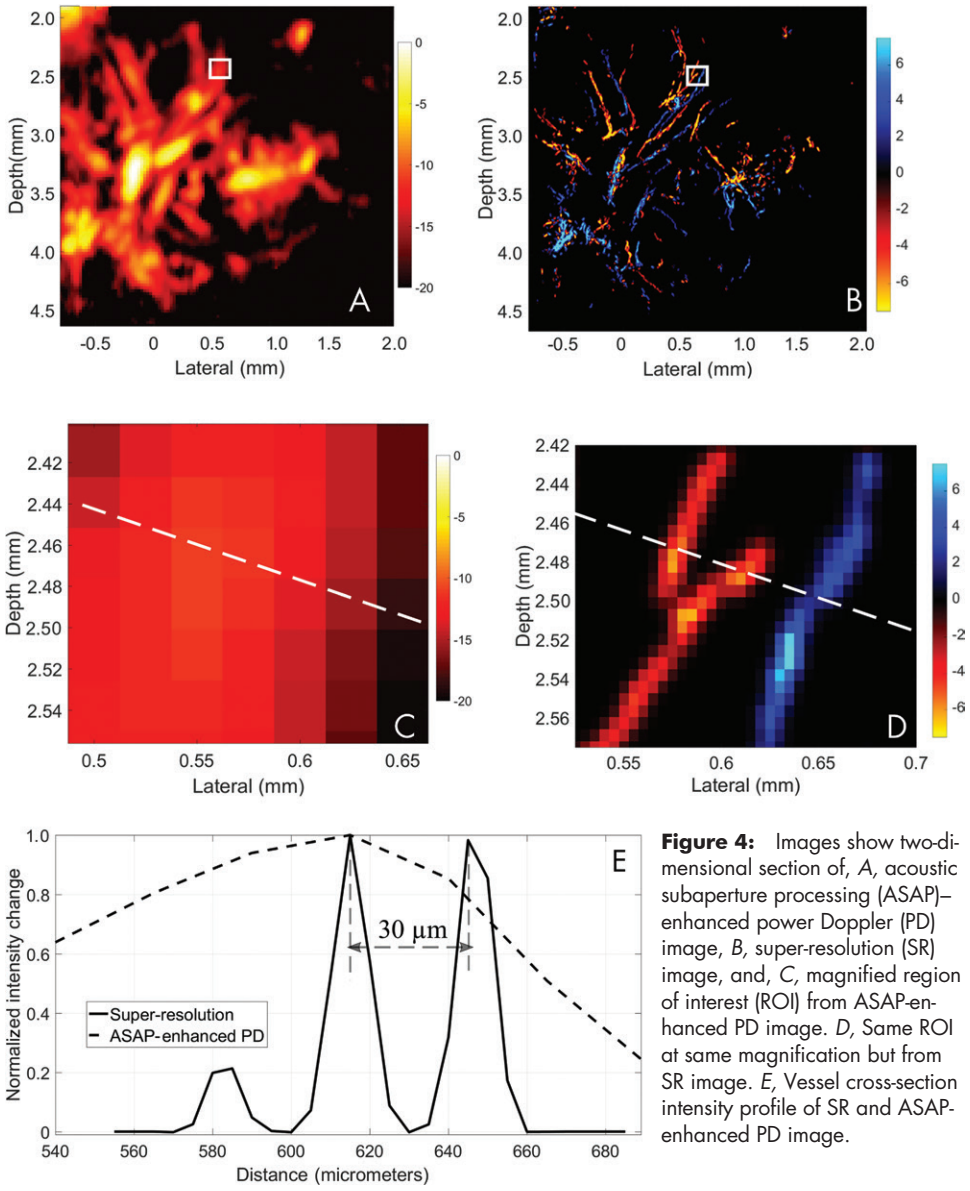

Figure 4: Images show two-dimensional section of, *A*, acoustic subaperture processing (ASAP)–enhanced power Doppler (PD) image, *B*, super-resolution (SR) image, and, *C*, magnified region of interest (ROI) from ASAP-enhanced PD image. *D*, Same ROI at same magnification but from SR image. *E*, Vessel cross-section intensity profile of SR and ASAP-enhanced PD image.

reduced noise level compared with PD. The ASAP-enhanced color Doppler images show color-coded flow directions.

SR Images

Two-dimensional SR image sections are shown in Figure 2. Detailed microvasculature is clearly visible in the SR images (Fig 2, *A*), unlike the PD images. Figure 2, *B* provides the color-encoded SR velocity maps of two-dimensional sections. The flow directions depicted in SR velocity maps (Fig 2, *B*) and those measured by using ASAP-enhanced color Doppler images were judged qualitatively to be similar (Fig 1, *C*).

Two-dimensional Projection of Three-dimensional Vasculature in LN

Figure 3 displays two-dimensional projections of three-dimensional information in the Doppler and SR images over 17 scanning positions, which cover 1.7-mm thickness. Figure 3, *A* gives the maximum intensity projection (or MIP) of ASAP-enhanced PD images for the two different LNs. The MIP of ASAP-enhanced color Doppler images are shown in Figure 3, *B*. For the MIP SR images shown in Figure 3, *C*, the hue represents the depth of the plane with the maximum intensity and saturation represents the number of microbubbles localized at that plane. This depth-based coloring of SR projection images revealed the complex three-dimensional microvascular structure of the LN. Velocity color-coded MIP projections of SR velocity are shown in Figure 3, *D*, in which the speed and direction correspond well to those visualized by using ASAP-enhanced Color Doppler (see image in Fig 3, *B*).

Quantification of Resolution and Velocity Distribution

Figure 4 illustrates the resolution improvement of the SR image over the ASAP-enhanced PD image. Figure 4, *A* and Figure 4, *B* show a two-dimensional ASAP-enhanced PD image and the corresponding two-dimensional SR image, respectively. Figure 4, *C* and Figure 4, *D* show higher magnification of the same region of interest. As illustrated in Figure 4, *D*, branched vessels are clearly identified and resolved from a third vessel with flow in the opposite direction; it is impossible to distinguish this in the ASAP-enhanced PD image (Fig 4, *C*). From the image intensity cross-sectional profiles (Fig 4, *E*), microvessels that are 30 μm apart can be clearly resolved in the SR image but are not separable in the ASAP-enhanced PD image.

Vessel size distribution measured on the PD and SR images from the two LNs are given in Figure 5. The size distributions from the two LNs agree well. The apparent size of most vessels in the SR image are below 80 μm, whereas most of those obtained by using ASAP-enhanced PD are larger between 100–250 μm. There are significant differences in vessel size distribution between PD and SR ($P < .001$ for LN1 thin vessels, $P < .001$ for lymph node 1 thick vessels, $P < .001$ for lymph node 2 thin vessels, and $P < .001$ for lymph node thick vessels).

The histograms showing blood flow velocity distributions in the two LNs can be seen in Figure 6. The distributions from the two LNs agree well, and the majority of velocities range from 0.1 mm/sec to 5 mm/sec in both LNs.

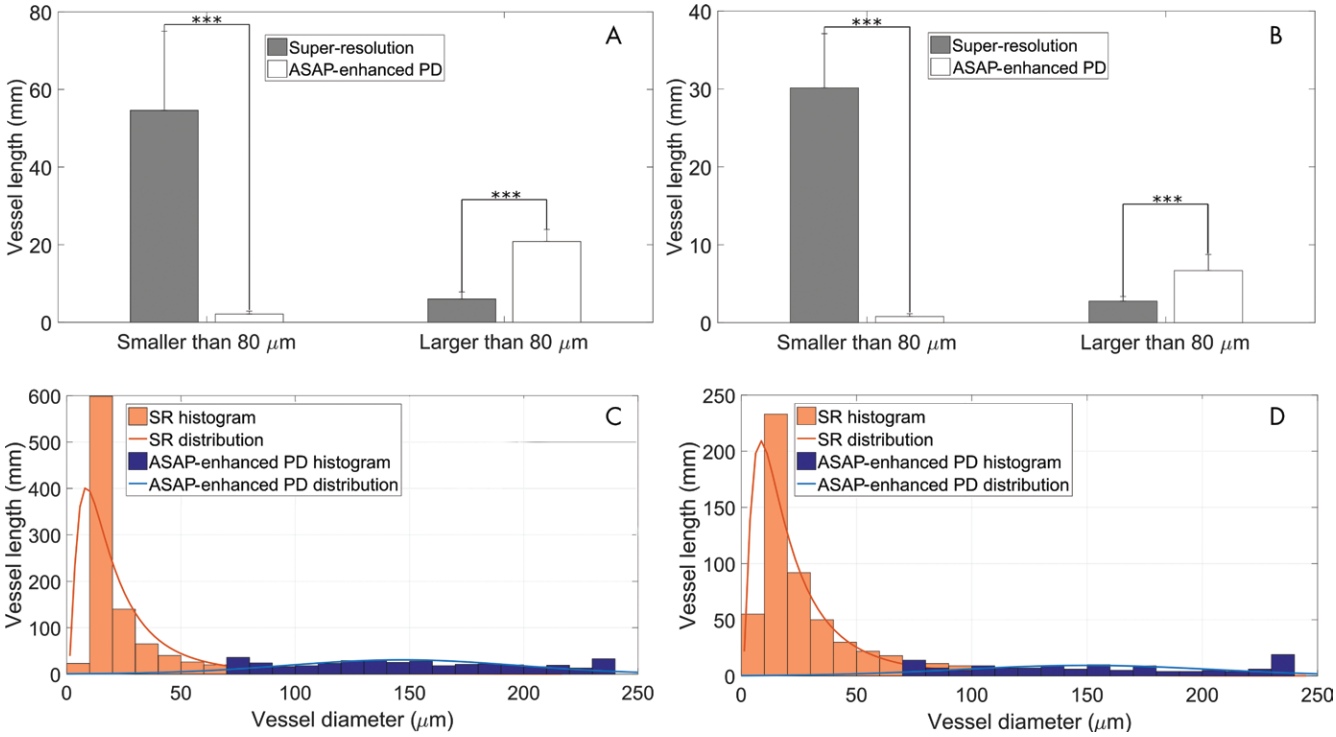

Figure 5: *A–D,* Graphs show comparison of detected vessel size distribution by using super-resolution (SR) and acoustic subaperture processing (ASAP)–enhanced power Doppler (PD) images. *A* and *B* are from two different lymph nodes. Vessel size distribution was assessed with Student paired *t* test. *** = $P < .001$.

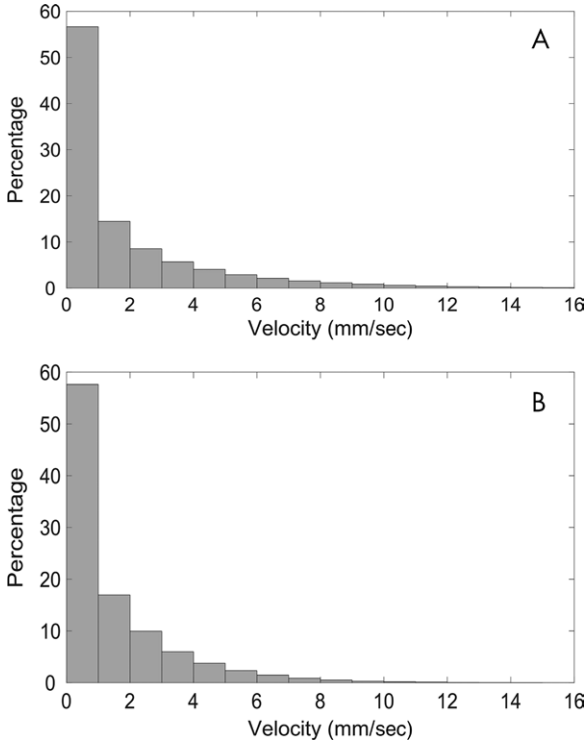

Figure 6: Histograms show blood flow velocity. *A* and *B* are from two different lymph nodes.

Figure E2 (online) shows the three-dimensional vasculature and the distribution of vessel diameter obtained from the micro-CT scan.

Discussion

In our study, we introduce super-resolution (SR) US imaging for three-dimensional visualization of lymph node (LN) vasculature in rabbit LNs in vivo. By using this technique, we achieved a spatial resolution sufficient to resolve LN microvessels 30 μm apart, a 15-fold improvement over existing Doppler techniques. Indeed, vessels smaller than 80 μm can only be resolved by using SR. We also generated SR blood flow maps. To our knowledge, this is the first use of in vivo SR US imaging of LNs that demonstrates the ability to provide detailed information on the morphology and dynamics of nodal microvasculature.

The ability to image at subdiffraction limit resolution in vivo, which could have substantial implications in the clinical management of patients with cancer. The standard method for LN staging is surgical excision and histopathologic assessment, despite the fact that many patients with cancer do not have LN metastases at the time of diagnosis (31). Surgical procedures involving LN removal can result in complications such as infection and long-term problems including lymphoedema, sensory loss, and weakness (32). Hence, a preoperative and noninvasive alternative is needed to accurately identify and quantify metastatic LNs. In addition, morphologic and functional abnormalities in tumor-draining LN microvessels may also be reliable early biomarkers of metastatic potential. Our study demonstrates the ability of this imaging technique to monitor microscopic changes in blood microcirculation, which could form the basis of noninvasive staging. Furthermore, because the test is repeatable, our methods allow assessment of dynamic responses in

microvascular and lymphatic vessels during therapy and could be a powerful tool for treatment monitoring.

Although the importance of visualizing and quantifying LN blood vessels is known, LN microvasculature is a largely unexplored area due to the resolution and contrast requirements. Several attempts have been made at quantifying LN vasculature. Kelch et al (33) used a confocal-based imaging platform called an extended-volume imaging system to scan and quantify blood vessels in a mouse LN. Kumar et al (34) used optical projection tomography and light sheet microscopy to image high-endothelial venules in optically cleared mouse popliteal LNs. However, both of these imaging techniques are invasive. Our SR US imaging is noninvasive and can be achieved with existing clinical scanners while not limited by the trade-off between resolution and penetration depth.

Our study had some limitations. The mechanical scanning method used in our study only offered in-plane SR, restricting the resolution in the third (elevational) dimension to the diffraction limit. This restriction can be overcome by using a two-dimensional matrix array to perform full three-dimensional SR US imaging. Another limitation of mechanical scanning is the long acquisition time required to obtain sufficient bubble data in each individual plane. Matrix array transducers can address this challenge, providing volumetric SR with much less acquisition time and maximum spatial resolution. The feasibility of three-dimensional ultrafast US imaging of tissue (35) and blood vessels (36) by using two-dimensional matrix probes has been demonstrated in humans in vivo. In addition, the micro-CT scan was performed separately on a third rabbit LN. It was not possible to perform the micro-CT scan in the same rabbit as the US scan due to the practical constraint.

In conclusion, our study demonstrates the feasibility of three-dimensional super-resolution US imaging of lymph node (LN) vascular structure and flow in vivo. The technique could potentially impact the management of a wide range of LN-related disease, including cancer.

Acknowledgment: The authors would like to thank Professor James E. Moore, Jr for advice.

Author contributions: Guarantors of integrity of entire study, J.Z., E.M.R., S.H., K.R., M.X.T.; study concepts/study design or data acquisition or data analysis/interpretation, all authors; manuscript drafting or manuscript revision for important intellectual content, all authors; approval of final version of submitted manuscript, all authors; agrees to ensure any questions related to the work are appropriately resolved, all authors; literature research, J.Z., E.M.R., S.H., C.H.L., K.C.J., C.D., R.J.E., M.X.T.; clinical studies, C.H.L., A.L.; experimental studies, J.Z., E.M.R., S.H., K.R., C.H.L., B.C., A.L., P.D.W., M.X.T.; statistical analysis, J.Z., S.H., C.H.L., B.C., K.C.J., C.D., M.X.T.; and manuscript editing, all authors

Disclosures of Conflicts of Interest: **J.Z.** disclosed no relevant relationships. **E.M.R.** disclosed no relevant relationships. **S.H.** disclosed no relevant relationships. **K.R.** disclosed no relevant relationships. **C.H.L.** disclosed no relevant relationships. **B.C.** disclosed no relevant relationships. **K.C.** disclosed no relevant relationships. **A.L.** disclosed no relevant relationships. **K.C.J.** disclosed no relevant relationships. **G.Z.** disclosed no relevant relationships. **J.B.** disclosed no relevant relationships. **C.D.** disclosed no relevant relationships. **R.J.E.** disclosed no relevant relationships. **P.D.W.** disclosed no relevant relationships. **M.X.T.** Activities related to the present article: disclosed no relevant relationships. Activities not related to the present article: has grants/grants pending with Heptares. Other relationships: disclosed no relevant relationships.

References

1. Stoll S, Delon J, Brotz TM, Germain RN. Dynamic imaging of T cell-dendritic cell interactions in lymph nodes. Science 2002;296(5574):1873–1876.
2. Girard JP, Moussion C, Förster R. HEVs, lymphatics and homeostatic immune cell trafficking in lymph nodes. Nat Rev Immunol 2012;12(11):762–773.
3. Rovera F, Fachinetti A, Rausei S, et al. Prognostic role of micrometastases in sentinel lymph node in patients with invasive breast cancer. Int J Surg 2013;11(Suppl 1):S73–S78.
4. Brown M, Assen FP, Leithner A, et al. Lymph node blood vessels provide exit routes for metastatic tumor cell dissemination in mice. Science 2018;359(6382):1408–1411.
5. Pereira ER, Kedrin D, Seano G, et al. Lymph node metastases can invade local blood vessels, exit the node, and colonize distant organs in mice. Science 2018;359(6382):1403–1407.
6. Wakisaka N, Hasegawa Y, Yoshimoto S, et al. Primary tumor-secreted lymphangiogenic factors induce pre-metastatic lymphvascular niche formation at sentinel lymph nodes in oral squamous cell carcinoma. PLoS One 2015;10(12):e0144056.
7. Ferris RL, Lotze MT, Leong SPL, Hoon DSB, Morton DL. Lymphatics, lymph nodes and the immune system: barriers and gateways for cancer spread. Clin Exp Metastasis 2012;29(7):729–736.
8. Grills IS, Kestin LL, Goldstein N, et al. Risk factors for regional nodal failure after breast-conserving therapy: regional nodal irradiation reduces rate of axillary failure in patients with four or more positive lymph nodes. Int J Radiat Oncol Biol Phys 2003;56(3):658–670.
9. Sharma N, Cox K. Axillary nodal staging with contrast-enhanced ultrasound. Curr Breast Cancer Rep 2017;9(4):259–263.
10. Macis G, Cina A, Pedicelli A, Restaino G, Molinari F. Lymph node imaging: from conventional radiology to diagnostic imaging. Rays 2000;25(4):399–417.
11. Viessmann OM, Eckersley RJ, Christensen-Jeffries K, Tang MX, Dunsby C. Acoustic super-resolution with ultrasound and microbubbles. Phys Med Biol 2013;58(18):6447–6458.
12. Desailly Y, Couture O, Fink M, Tanter M. Sono-activated ultrasound localization microscopy. Appl Phys Lett 2013;103(17):174107.
13. Christensen-Jeffries K, Browning RJ, Tang MX, Dunsby C, Eckersley RJ. In vivo acoustic super-resolution and super-resolved velocity mapping using microbubbles. IEEE Trans Med Imaging 2015;34(2):433–440.
14. Errico C, Pierre J, Pezet S, et al. Ultrafast ultrasound localization microscopy for deep super-resolution vascular imaging. Nature 2015;527(7579):499–502.
15. Ackermann D, Schmitz G. Detection and tracking of multiple microbubbles in ultrasound b-mode images. IEEE Trans Ultrason Ferroelectr Freq Control 2016;63(1):72–82.
16. Bar-Zion A, Tremblay-Darveau C, Solomon O, Adam D, Eldar YC. Fast vascular ultrasound imaging with enhanced spatial resolution and background rejection. IEEE Trans Med Imaging 2017;36(1):169–180.
17. Song P, Trzasko JD, Manduca A, et al. Improved super-resolution ultrasound microvessel imaging with spatiotemporal nonlocal means filtering and bipartite graph-based microbubble tracking. IEEE Trans Ultrason Ferroelectr Freq Control 2018;65(2):149–167.
18. Harput S, Christensen-Jeffries K, Li Y, et al. Two Stage Sub-Wavelength Motion Correction in Human Microvasculature for CEUS Imaging. 2017 IEEE Int Ultrason Symp IUS. 2017; 1–1.
19. Opacic T, Dencks S, Theek B, et al. Motion model ultrasound localization microscopy for preclinical and clinical multiparametric tumor characterization. Nat Commun 2018;9(1):1527.
20. Dencks S, Piepenbrock M, Opacic T, et al. Clinical pilot application of super-resolution US imaging in breast cancer. IEEE Trans Ultrason Ferroelectr Freq Control 2018 Sep 24 [Epub ahead of print].
21. Zhang G, Harput S, Lin S, et al. Acoustic wave sparsely activated localization microscopy (AWSALM): super-resolution ultrasound imaging using acoustic activation and deactivation of nanodroplets. Appl Phys Lett 2018;113(1):014101.
22. Lin F, Shelton SE, Espíndola D, Rojas JD, Pinton G, Dayton PA. 3-D ultrasound localization microscopy for identifying microvascular morphology features of tumor angiogenesis at a resolution beyond the diffraction limit of conventional ultrasound. Theranostics 2017;7(1):196–204.
23. Christensen-Jeffries K, Brown J, Aljabar P, Tang M, Dunsby C, Eckersley RJ. 3-D in vitro acoustic super-resolution and super-resolved velocity mapping using microbubbles. IEEE Trans Ultrason Ferroelectr Freq Control 2017;64(10):1478–1486.
24. O'Reilly MA, Hynynen K. A super-resolution ultrasound method for brain vascular mapping. Med Phys 2013;40(11):110701.

25. LabDiet - rabbits. https://www.labdiet.com/Products/StandardDiets/Rabbits/index.htm. Accessed January 15, 2019.
26. Lin S, Zhang G, Leow CH, Tang MX. Effects of microchannel confinement on acoustic vaporisation of ultrasound phase change contrast agents. Phys Med Biol 2017;62(17):6884–6898.
27. Stanziola A, Leow CH, Bazigou E, Weinberg PD, Tang MX. ASAP: super-contrast vasculature imaging using coherence analysis and high frame-rate contrast enhanced ultrasound. IEEE Trans Med Imaging 2018;37(8):1847–1856.
28. Bayat M, Fatemi M, Alizad A. Background removal and vessel filtering of noncontrast ultrasound images of microvasculature. IEEE Trans Biomed Eng 2019;66(3):831–842.
29. Frangi AF, Niessen WJ, Vincken KL, Viergever MA. Multiscale vessel enhancement filtering. In: Wells WM, Colchester A, Delp S, eds. Med Image Comput Comput-Assist Interv — MICCAI'98. Berlin, Germany: Springer, 1998; 130–137. http://link.springer.com/10.1007/BFb0056195. Accessed September 29, 2018.
30. BahadarKhan K, A Khaliq A, Shahid M. A morphological hessian based approach for retinal blood vessels segmentation and denoising using region based Otsu thresholding. PLoS One 2016;11(7):e0158996 [Published correction appears in PLoS One 2016;11(9):e0162581.] https://doi.org/10.1371/journal.pone.0158996.
31. Krag DN, Anderson SJ, Julian TB, et al. Sentinel-lymph-node resection compared with conventional axillary-lymph-node dissection in clinically node-negative patients with breast cancer: overall survival findings from the NSABP B-32 randomised phase 3 trial. Lancet Oncol 2010;11(10):927–933.
32. Mansel RE, Fallowfield L, Kissin M, et al. Randomized multicenter trial of sentinel node biopsy versus standard axillary treatment in operable breast cancer: the ALMANAC Trial. J Natl Cancer Inst 2006;98(9):599–609.
33. Kelch ID, Bogle G, Sands GB, Phillips AR, LeGrice IJ, Dunbar PR. Organ-wide 3D-imaging and topological analysis of the continuous microvascular network in a murine lymph node. Sci Rep 2015;5:16534.
34. Kumar V, Chyou S, Stein JV, Lu TT. Optical projection tomography reveals dynamics of HEV growth after immunization with protein plus CFA and features shared with HEVs in acute autoinflammatory lymphadenopathy. Front Immunol 2012;3:282.
35. Provost J, Papadacci C, Arango JE, et al. 3D ultrafast ultrasound imaging in vivo. Phys Med Biol 2014;59(19):L1–L13.
36. Provost J, Papadacci C, Demene C, Gennisson JL, Tanter M, Pernot M. 3-D ultrafast Doppler imaging applied to the noninvasive mapping of blood vessels in vivo. IEEE Trans Ultrason Ferroelectr Freq Control 2015;62(8):1467–1472.